Origin of surface-induced visible light absorption of nanostructured diamond

A. Bellucci,* A. Chemin, T. Petit, E. Bolli, V. Valentini, B.L. Cotts, A. Salleo, M. Girolami, S. Orlando, and D.M. Trucchi

Received: 14 March 2025 / Revised: 17 June 2025 / Accepted: 1 July 2025 / Published online: 29 October 2025

Surface nanotextured diamond, named "black diamond," absorbs efficiently visible light. This feature allows this material to be used in solar devices, such as the *p/i/n* photocathode under study in this work. Using optical and x-ray surface-sensitive spectroscopy techniques, this study establishes a correlation between the material's optical properties and its chemical structure to elucidate the nature of light absorption and photocarriers' generation. The analysis reveals that the surface states in the very first atomic layer of the diamond, such as carbon sp^2 reconstruction states and carbon oxygen bounds at 1.25 and 2.5 eV with respect to the maximum of the valence band, respectively, are the key factors for the enhancement of the visible light absorption with respect to pristine samples. These defects, together with a collective effect induced by the diffraction light trapping, could be useful for using black diamond in solar applications by exploiting the increase in the visible light absorption.

Impact statement

Diamond, an ultrawide bandgap semiconductor with an energy bandgap of 5. 47 eV, possesses exceptional thermal, mechanical, and electronic properties, making it a promising material for a wide range of applications. However, its intrinsic nature renders diamond natively visible blind, limiting its potential in solar-energy applications. Surface texturing using ultrashort laser pulses offers a way to enable diamond's utilization in sunlight conversion. Nonetheless, it is crucial to understand the effects induced by laser treatments on its surface to tailor and optimize it as an active solar material. This study highlights the critical role of sp^2 defects formed in the uppermost layers of monodimensional laser-induced periodic surface structures (1D LIPSSs). These defects play a primary role in absorbing subbandgap photons. The recognition of the direct involvement of surface defects in the absorption mechanism paves the way for the development of highly efficient and fine- tuned nanotextured surfaces, designed to maximize the presence of these beneficial defects.

Introduction

Photon-enhanced thermionic emission (PETE) is a physical mechanism that finds its suitable application in the conversion of concentrated solar radiation, because it is based on the use of both photon absorption and thermal effects for enhancing the electronic population available for the electrons' emission.[1] Unlike conventional thermionic energy converters, PETE cathodes are based on *p*-type semiconductors to exploit both photoelectric and thermalization effects for enabling an enhanced electrons' emission and need a low electron affinity, whereas the work function value is important to establish the device output voltage (i.e., the difference between the work functions of the cathode and the anode). Combined to secondary stages of conversion, converters based on PETE can theoretically achieve extremely high conversion efficiency values, up to 70.4% at 1000 suns, thus overcoming both Shockley–Queisser and Carnot limits for single-junction photovoltaic cells and thermal engines, respectively.[2] Since the introduction of the PETE concept, structures based on the use of III–V semiconductors are mainly analyzed for practical implementation of cathodes.[3] However, they face

A. Bellucci, Istituto di Struttura della Materia (ISM), Sez. Montelibretti, DiaTHEMA Lab, Consiglio Nazionale delle Ricerche (CNR), 00015 Monterotondo (RM), Italy; alessandro.bellucci@cnr.it
A. Chemin, Helmholtz-Zentrum Berlin für Materialien und Energie GmbH, 12489 Berlin, Germany
T. Petit, Helmholtz-Zentrum Berlin für Materialien und Energie GmbH, 12489 Berlin, Germany
E. Bolli, Istituto di Struttura della Materia (ISM), Sez. Montelibretti, DiaTHEMA Lab, Consiglio Nazionale delle Ricerche (CNR), 00015 Monterotondo (RM), Italy
V. Valentini, Istituto di Struttura della Materia (ISM), Sez. Montelibretti, DiaTHEMA Lab, Consiglio Nazionale delle Ricerche (CNR), 00015 Monterotondo (RM), Italy
B.L. Cotts, Department of Materials Science and Engineering, Stanford University, Stanford, USA; Department of Chemistry and Biochemistry, Middlebury College, Middlebury, USA
A. Salleo, Department of Materials Science and Engineering, Stanford University, Stanford, USA
M. Girolami, Istituto di Struttura della Materia (ISM), Sez. Montelibretti, DiaTHEMA Lab, Consiglio Nazionale delle Ricerche (CNR), 00015 Monterotondo (RM), Italy
S. Orlando, Istituto di Struttura della Materia (ISM), Sez. Tito Scalo, Consiglio Nazionale delle Ricerche (CNR), 85050 Tito Scalo (PZ), Italy
D.M. Trucchi, Istituto di Struttura della Materia (ISM), Sez. Montelibretti, DiaTHEMA Lab, Consiglio Nazionale delle Ricerche (CNR), 00015 Monterotondo (RM), Italy
*Corresponding author
doi:10.1557/s43577-025-00971-2

challenges related to stability at medium-high temperatures and in the reduction of the electron affinity. As an alternative of these structures, the concept of defect-engineered diamond was introduced some years ago for the formation of *p/i* or *p/i/n* cathodes obtained through ultrashort laser pulse technology that can enable charge-carriers' photogeneration in diamond exploiting the PETE conversion with solar radiation.[4] Ultrashort laser pulses were used to form one-dimensional (1D) laser-induced periodic surface structures (LIPSS) on diamond,[5] as well as pseudo-two-dimensional (2D)[6] or engineered 2D LIPSS.[7] The nanotextured diamond surface acts as an absorbing layer, able to produce photo-charge carriers by photon absorption. Additionally, a buried *p*-type layer underneath the surface is obtained by boron implantation to form a selective contact for holes to minimize the carriers' recombination. Localized graphitic microcolumns are created within the diamond bulk to reduce the device's series resistance and facilitate the transport of photoelectrons from the absorbing layer toward the emitting sites. Finally, the functionalization of the emitting diamond surface through specific terminations, such as hydrogenation, is used to tune the surface electron affinity while the incorporation of nitrogen doping atoms can be used to reduce the work function. Among these features, the specific absorption properties of the nanostructured layer, named black diamond (BD), and the origin of this property are fundamental to investigate. Such layer does not act only as an antireflective coating, but also absorbs photons and promotes photoelectrons to the conduction band. An enhancement of the photoelectronic gain for subbandgap photons up to 5 and 50 times at wavelength of 500 nm (close to the maximum peak of the solar spectrum) was reported for 1D and psuedo-2D treated diamond surfaces, due to the formation of defects states into the diamond bandgap.[6] However, the correlation between this enhancement and the physical and chemical nature of possible defects was never clarified.

The presence of inter-bandgap defect states and surface states have been shown to be excited by visible light on nanostructured boron-doped diamonds, leading to charge separation.[8] In our material, similar processes could happen and remain to be investigated. Considering that the mesoscale collective effects contribute significantly to enhance the absorption across a broad range of wavelengths by the diffraction effect of light trapping, identifying the presence and positions of specific bandgap defects contributing to photoelectron emission requires a technique capable of isolating these effects. Photothermal deflection spectroscopy (PDS) is particularly well suited for this purpose, as it enables the disentanglement from the surface morphology. Moreover, considering that the effects induced by the laser nanotexturing are localized in the first material atomic layers, surface-sensitive techniques must be used to correlate change of the absorption coefficient with structural and chemical features. Therefore, tip-enhanced Raman spectroscopy (TERS), x-ray absorption spectroscopy (XAS), and depth-resolved x-ray photoelectron spectroscopy (XPS) were used for investigating the black diamond surfaces. This study aims to reveal the nature of the surface defect states involved in the absorption and photogeneration process in 1D-LIPSS black diamond, as a preliminary work to understand how to improve and further engineer the fabrication of related energy-conversion devices for practical applications.

Materials and methods

A Ti:Sapphire femtosecond laser (100-fs duration, 800-nm wavelength, 1-kHz repetition rate) was used for the 1D-LIPSS fabrication. The beam was perpendicularly focused onto the surface of commercially available (Element Six Ltd.) single-crystal diamond (SCD) standard-grade plates ($4.5 \times 4.5 \times 0.5$ mm^3, double-side polished, surface roughness <30 nm, ⟨100⟩ crystallographic plane), which were positioned on a motorized sample holder in a high vacuum chamber ($<10^{-7}$ mbar), allowing the sample precise positioning and laser-beam scanning. The impinging radiation dose, defined as the energy of a single pulse multiplied by the number of pulses impinging the sample surface unit, was fixed to 2.1 kJ cm^{-2}, according to the conditions reported in Reference 9. After laser processing, a strongly oxidizing solution ($H_2SO_4/HClO_4/HNO_3$ in equal volume at the boiling point) was used with the aim to remove any debris and graphitic content produced by the treatment. This chemical etching does not affect the diamond surface morphology but oxidizes the surface.

Additionally, the investigated samples were fabricated considering the other following technological steps: (1) implantation of B ions under the nanotextured surface for the formation of a buried *p*-type layer, according to our previous work:[10] boron dose of 1×10^{15} cm^{-2} and implantation kinetic energy of 40 keV. The estimated boron concentration is ~3×10^{20} cm^{-3} with a peak at ~90 nm below the surface; (2) fs laser-induced distributed contacts for reducing device series resistance consisting of an array of 10,000 columns (100×100 columns, pitch of 40 µm) within the diamond plates, fabricated according to an optimized graphitization recipe reported in Reference 11. The fs-laser system used for the fabrication is the same allowing the surface nanostructuring.

Raman measurements were carried out using a Horiba Scientific LabRam HR Evolution confocal spectrometer equipped with a 100-mW Oxxius ($\lambda_{exc} = 633$ nm) laser source and a computerized XY-table, an electron-multiplier CCD detector, and an Olympus U5RE2 microscope with a 50× long working distance objective (laser spot on the sample surface is 1.3 µm) with a numerical aperture (NA) of 0.5, and a grating with 300 grooves/mm were used.

TERS analyses were performed by integrating the previously described Raman spectroscopy system with an atomic force microscopy (AFM) system based on an OmegaScope platform (HORIBA Ltd., Kyoto, Japan). A laser excitation

source was specifically adapted for TERS by directing it through a dedicated optical path, allowing precise focusing on the apex of a silver-coated tip (Omni TERS-SNC-Ag-3, AppNano, Mountain View, Calif.). This precise alignment was achieved with the assistance of dual optical microscopes (top and side view) controlled by the AIST-NT v3.5 SPM control software. This configuration was critical for generating enhanced near-field effects necessary for TERS measurements, overcoming the spatial resolution and surface sensitivity limitations inherent to conventional Raman spectroscopy.[12–14] The TERS measurements were conducted with an accumulation time of 10 s per spectrum and a laser power setting of 3.2 percent. Spectra were acquired at intervals of 100 nm across a total scanning area of 2.5 × 2.5 µm, for which a preliminary AFM map had been obtained to characterize the morphology of the region of interest, ensuring precise targeting of specific features within the sample.

Photothermal deflection spectroscopy (PDS) spectra were measured using a home-built instrument as previously described by Vandewal et al.[15] Monochromatized light from either a 150-W Xenon or a 100 W halogen lamp is modulated at 2-Hz frequency with a mechanical chopper and then split to be separately focused onto the sample and a pyroelectric detector. Samples were immersed in the deflection medium of degassed and filtered perfluorohexane (C6F14, 3M Fluorinert FC-72). A HeNe laser probe was aligned both perpendicularly to the pump beam and parallel to the sample surface, so that its deflection could be measured by a position-sensitive Si detector using a lock-in amplifier.

X-ray absorption spectroscopy (XAS) experiments were conducted under an ultrahigh vacuum at the HE-SMG beamline, situated at BESSY-II electron storage ring in Berlin, Germany. The measurements were carried out in the electron yield (EY) mode, wherein the incident photon energy was varied while concurrently recording the emitted electrons from the sample. The beamline was optimized for near-edge x-ray absorption fine structure (NEXAFS) at the C edge by mitigating potential carbon contamination originating from the optical elements within the beamline. Spectral data normalization was carried out by accounting for the incident photon flux and did not require further background corrections. The energy resolution of the monochromator, within the vicinity of the C 1s (~285 eV) x-ray absorption edges, approximated to ~70 meV. The x-ray energy scale was calibrated against the energy positions of the primary narrow peak observed in the C 1s absorption spectrum of highly ordered pyrolytic graphite (HOPG), which manifested at approximately ~285.45 eV. Oxidized single-crystal (O-SC) diamond was used as reference samples. This is an intrinsic diamond measuring 3 × 3 × 0.2 mm^3, consisting of a chemical vapor deposition (CVD)-grown substrate (optical grade, approximately 1-ppm P1 nitrogen) with a 15-µm ultrapure diamond layer (electronic grade, no detectable contamination) overgrowth. The oxidized surface was prepared through wet chemical treatment in a 3:1 mixture of sulfuric acid and nitric acid for 1.5 h at elevated temperatures.

On the same beamline, x-ray photoelectron spectra (XPS) were measured for various excitation energies to probe various depth. The Scienta Omicron R3000 analyzer with a radius of 135 mm and a slit width of 3 mm and a pass energy of 50 V leads to a total resolution of about 0.6 eV for an excitation energy of 335 eV. The binding energy (BE) has been shifted to take into consideration variation of the homogeneous charging depending on the excitation energy so that the sp^3 peak is centered at 285 eV.

Results and discussion

A typical black diamond surface under investigation is shown in **Figure** 1a, c. The formation of 1D-LIPSS on diamond induces a periodicity of 170 ± 10 nm (Figure 1b) and length of uninterrupted grooves up to some micrometers, as already reported in the past by scanning electron microscopy.[5,16]

TERS measurements were performed on the BD sample and the pristine one. With respect to conventional Raman spectroscopy, TERS analysis is an extremely surface-sensitive technique and spatially resolved at the nanoscale. Generally, a TERS map allows to register confocal Raman spectra following the surface aspect shown by AFM, as well as to record specific Raman intensity signals to reveal chemical differences depending on morphology. TERS measurements have already been performed on nanodiamond[17] and nanocrystalline diamond (NCD) films,[18] highlighting significant differences between the far-field and near-field Raman spectra. For the NCD films, a correlation between morphological features and specific signals has been reported, following the intensity of the band along one axial direction. In the specific case of BD (**Figure** 2a), we found that there is no direct correlation between the morphological features of 1D-LIPSS structures and the recorded Raman signal, so that the nanostructuring results in a homogeneous surface chemistry despite strong morphology changes. As a result, an average analysis has been performed on the whole area considered. Figure 2b shows a comparison among the Raman spectra obtained using the conventional technique and the TERS measurements for both BD and pristine samples. It appears clear that the difference among the spectra arises from the enhanced contribution of the surface for the BD, where several hidden contributions come up from the upmost atomic layers, thus allowing the identification of a different behavior between bulk and surface. For BD, a completely different behavior can be observed: in fact, the distinguished diamond peak at 1332 cm^{-1}, which is clearly visible in the Raman spectrum, is overwhelmed by the D band (~1350 cm^{-1}) in the TERS spectrum. This means that locally the nanostructuring increases the defect density of states. On the other hand, for the pristine sample the TERS spectrum is very similar to that obtained from conventional

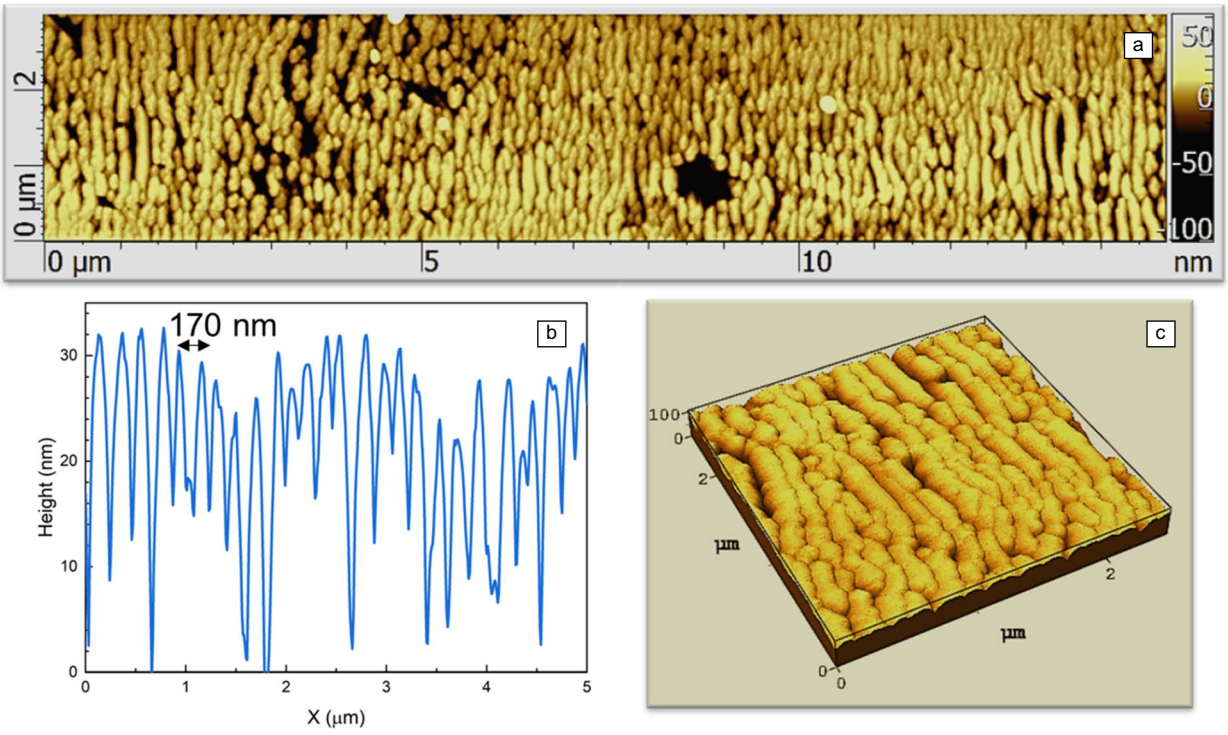

Figure 1. (a) Atomic force microscopy (AFM) image on large area (3 µm × 15 µm); (b) profile along a horizontal line of the height of the 1D-laser-induced periodic surface structures for detecting periodicity; (c) 3D AFM profile on small area.

Raman spectroscopy, thus indicating that the main response of the surface is correlated with that coming from the bulk.

All the surface Raman contributions of the BD are detailed in Figure 2c. In addition to the D band, which typically indicates the presence of defects and disorder for diamond systems,[19] the main peaks are the ν_3 signal at 1431 cm^{-1}, attributed in the nanodiamond films to trans-polyacetylene (t-PA) chains forming the grain boundaries, and the ν=C–C= modes associated with the 1365–1380 cm^{-1} and 1922 cm^{-1} bands.[20] It is important to note the presence of a band at 1543 cm^{-1}, which is largely downshifted with respect to the G-peak associated with C–C bonds as sp^2 hybridization (1580 cm^{-1}): this indicates that this kind of contribution is due to the t-PA conjugated carbon–carbon double bonds,[21] rather than to laser-induced graphite, the band of which is at lower wavenumbers when carbon is bonded with high disorder or is even amorphous.[22] Additionally, the band at 1225 cm^{-1} is a typical feature of the detonation nanodiamond,[23] confirmed also by the assignment of the surface-enhanced Raman spectroscopy measurements to the phonon density of states of diamond.[24] This occurs with very small diamond grains, and it indicates reduced grain size in the grooves formed by laser treatment. The appearance of these additional bands is directly correlated to surface-localized structural changes induced by the nanostructuring, which cannot be detected by conventional Raman. Moreover, a band at 1840 cm^{-1} is identified and assigned to C=O bonds. It is upshifted with respect to nanodiamond, but it is well known that the peak position increases as a function of the size of the diamond domains.[25]

Finally, the TERS analysis highlights that different nondiamond species are present on the surface, particularly associated with a large quantity of t-PA bonds, induced by the reduction of the diamond domain size at the upmost surface layers.

To validate the TERS analysis and examine the optical absorption induced by surface states formed by the laser treatment, XAS measurements were conducted at the C K-edge on BD and reference samples. XAS allows us to determine the position of unoccupied surface states, providing insight into their contribution to the capability of visible light absorption.

Figure 3a presents the pre-edge region of C K-edge (the entire XAS spectra at the C K-edge for BD and reference samples are shown in Supplementary information (SI) Figure S1). The core exciton peak at 289.3 eV can be used to determine the conduction-band minimum (CBM) of the diamond by adding the energy of the core exciton (~0.19 eV).[26] The position of the bulk valence-band maximum (VBM) is consequently determined considering a bandgap of 5.47 eV. In-between, each feature corresponds to the excitation of unoccupied states present at the diamond surface. The absorption at 285.2 eV is attributed to the C(1s) → $\pi^*_{C=C}$ transitions from sp^2 carbon bonds created by surface defects or graphene-like carbon.[27–29] The absorption at 286.5 eV corresponds to C(1s) → $\pi^*_{C=O}$ transitions from

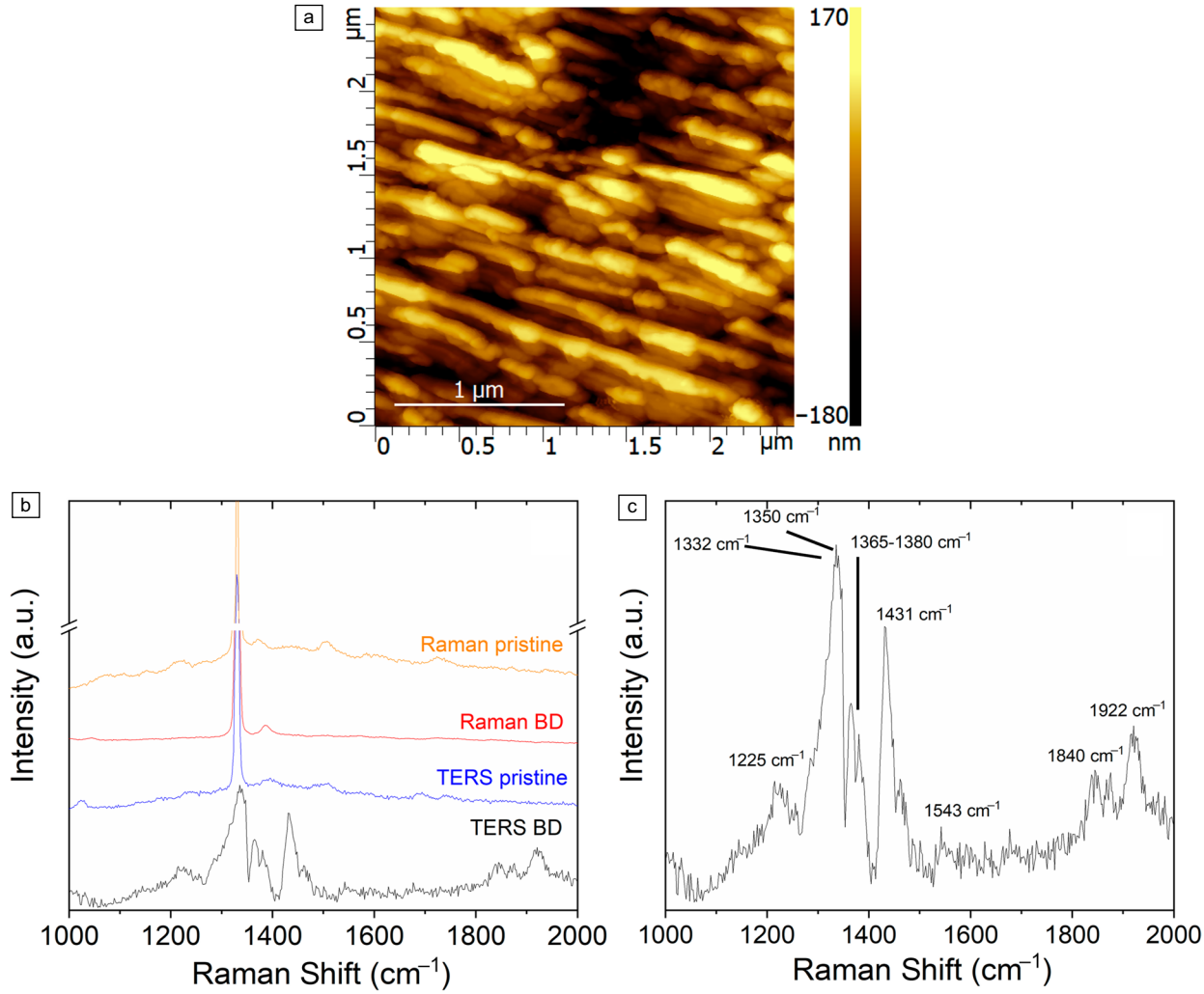

Figure 2. (a) Atomic force microscopy image of the black diamond (BD) sample on which tip-enhanced Raman spectroscopy (TERS) measurements were performed; (b) comparison of conventional Raman and TERS spectra for pristine and BD single-crystal diamond samples; (c) focus and assignments for the Raman spectra in TERS for BD sample.

carbonyl groups,[30] the signal at 287.8 eV corresponds to the C(1s) → σ* transition of carbon atoms bonded to hydrogen atoms (C–H),[31] and the shoulder at 288.7 eV corresponds to carbon atoms bonded to hydroxyl group (C–OH).[32] The BD sample shows increased pre-edge features compared to the reference single-crystals, highlighting increased amount of interband states as well as broad C(1s) → $\pi^*_{C=C}$ transitions centered at 285.1 eV. Similarly, the feature at 286.4 eV is shifted to lower energy compared to the usual C(1s) → $\pi^*_{C=O}$ transitions. The increased density of defects in the first few nanometers of the surface correlates well with the surface nanostructuring.

The surface states greatly influence the subbandgap absorption in diamond and the position of the characterized unoccupied states compared to the position of the VBM can be used to identify the optical transitions.[8] The strong absorption in the UV related to the band-to-band excitation of the diamond starts below the energy of the bandgap (5.47 eV) as transitions at lower energy involving indirect excitons and phonons are involved. For instance, the transitions at $E_g - E_x \pm h\nu_{LO/LA}$ where E_x and $h\nu_{LO/LA}$ are the energies of the indirect exciton (0.07 eV) and of the longitudinal optical and acoustic phonons (0.132 eV), respectively,[33] which were also observed by Surface PhotoVoltage (SPV).[8,34,35]

On the other hand, PDS measurements were conducted with the aim of identifying the presence of optically active subbandgap energy levels introduced by the laser treatment. This technique is based on the "mirage effect," exploiting the heat produced by the light absorption on a material surface.[36] In contrast to conventional transmission, these measurements can eliminate the effects of light scattering, thus allowing the evaluation of the absorption of local defects.[37] Furthermore, this method allows extrapolation of the absorption coefficient even in a spectral region in which the absorption is extremely low. Since black diamond films are surface nanostructured as

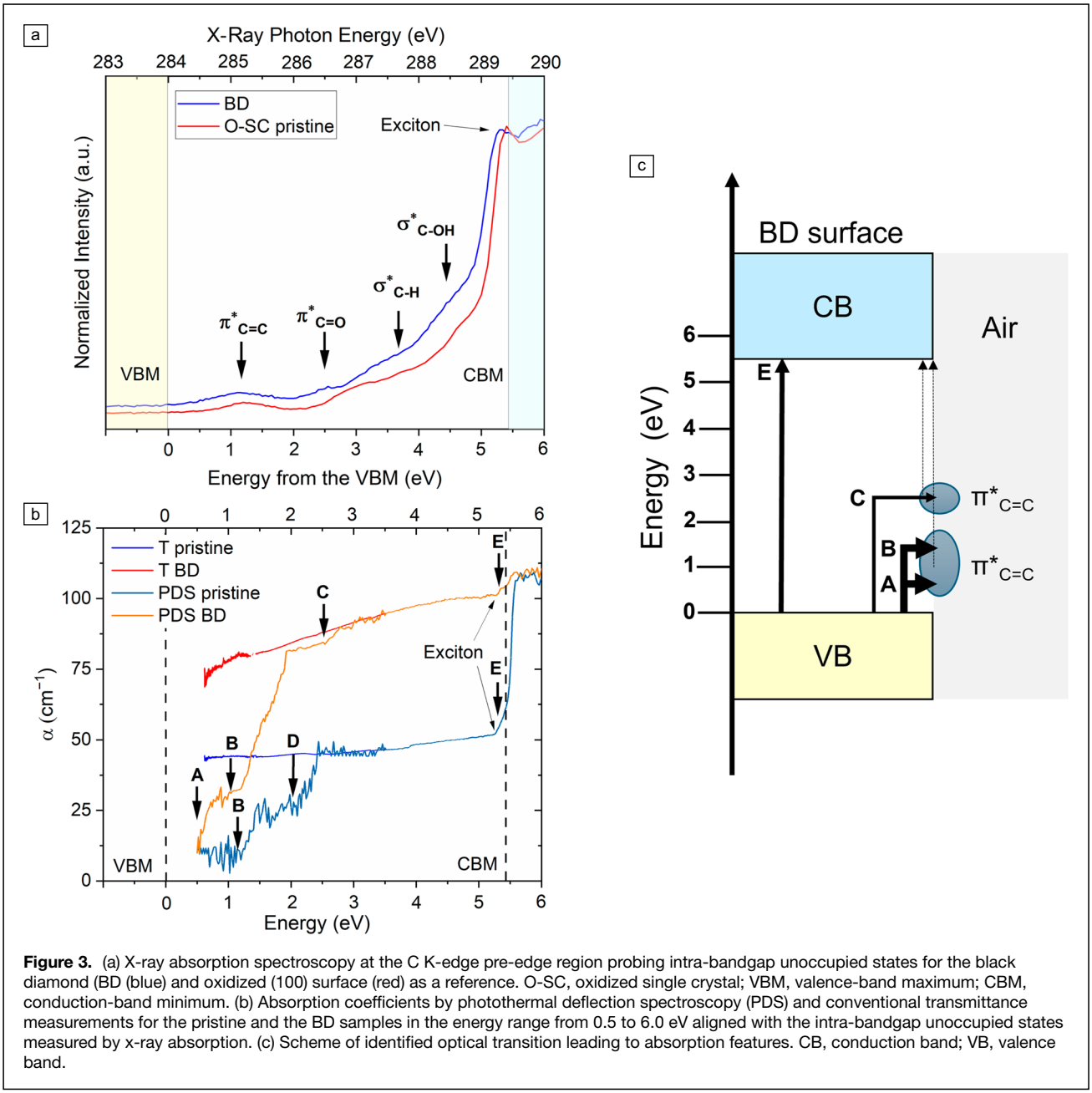

Figure 3. (a) X-ray absorption spectroscopy at the C K-edge pre-edge region probing intra-bandgap unoccupied states for the black diamond (BD (blue) and oxidized (100) surface (red) as a reference. O-SC, oxidized single crystal; VBM, valence-band maximum; CBM, conduction-band minimum. (b) Absorption coefficients by photothermal deflection spectroscopy (PDS) and conventional transmittance measurements for the pristine and the BD samples in the energy range from 0.5 to 6.0 eV aligned with the intra-bandgap unoccupied states measured by x-ray absorption. (c) Scheme of identified optical transition leading to absorption features. CB, conduction band; VB, valence band.

relief diffraction gratings, the antireflection properties represent the phenomenon dominating the optical behavior of the system, as occurs in nanostructured surfaces inspired by the "moth's eye" mechanisms.[38,39] PDS measurements are capable to disentangle this effect from the absorption of defect centers present in the bandgap or of band-to-band transitions.

Since the PDS characterization is performed at photon energies from 0.5 to 3.5 eV (the upper limit is due to the limitation of the light source), optical transmission measurements are used to determine the saturated value (S_0) achieved at wavelengths of complete absorption (over-bandgap) in order to obtain the absolute spectrum of the absorption coefficient α, according to the formula: $\alpha = -d^{-1} \times \ln(1 - S/S_0)$, where d is the sample thickness.[40] Figure 3b shows the absorption coefficient extracted from the PDS measurements (the raw data of which are shown in SI Figure S2). The transmittance measurements at energies higher than 3.5 eV are used to normalize the PDS values in the range above 3.5 eV and the curves of the pristine SCD sample displayed as a reference.

Considering the transmittance measurement, the absorption edge is clearly identified for the pristine SCD sample at the diamond bandgap (5.47 eV), with the value of α increasing from ~51 to ~106 cm^{-1}. Conversely, the BD SCD sample presents a transmittance (T) variation of α lower than 10% at the bandgap edge, highlighting the high absorption of subbandgap radiation. Conversely, the absorption coefficient extracted

from the PDS measurements shows evidence of a sharp optical transition in which α increases from 20 to 70 cm^{-1} for photon energies of ~1.25–1.3 eV and, by direct comparison with the pristine sample, which presents a very narrow transition as well, this boost is directly ascribable to the effect of the 1D-LIPSS formation. A similar defect level (located at ~1 eV) in CVD diamond films was suspected to be an acceptor level just above the valence-band maximum for the hole transition, for both intrinsic and boron-doped thin films.[41] Thus, the indication is that the laser treatment leads to an increase of the density of states around this exact energy level, which is associated in an enhanced absorption. Besides, since no specific features can be detected from the T spectrum, this observation clearly confirms that the diffraction effect is predominant for the BD absorption in the infrared range (wavelengths >620 nm), where α is quite high in T measurements with respect to the PDS ones (~79 and ~25 cm^{-1} at 1000 nm for T and PDS measurements, respectively). In addition to the main transition for the BD, it is possible to note the presence of other absorption features at different energies, such as ~0.5 and ~2.5–2.7 eV. In particular, the transition at ~0.5 eV is not observed in the pristine, which, on the other hand, presents a significant absorption between 1.5 and 2.5 eV. Therefore, although the present study does not provide a quantitative and absolute separation between defect-state absorption and morphology-induced light trapping, the PDS measurements enable the disentanglement of specific absorption centers from the collective contribution coming from the nanostructured surface. Interestingly, similar studies have been previously conducted on boron-doped nanocrystalline diamond[42] and CVD diamond containing nitrogen.[43] In both cases—analogous to the current findings on BD—optical absorption is primarily dominated by grain boundaries at the surface, which are rich in sp^2-bonded carbon (e.g., amorphous carbon or graphite). These sp^2-related states are responsible for the subbandgap optical transitions that govern light absorption in these materials.

By correlating PDS and XAS measurements, it is possible to identify the chemical nature of the states involved in the absorption mechanism, as shown in Figure 3b. The first observed transition at ~0.5 eV, named A, which is characteristic of BD, and the main absorption transition at ~1.25–1.3 eV, named B, match the energy of the excitation of a VB electron to a $\pi^*_{C=C}$ unoccupied states. As previously reported, the transition B is present on both the BD sample and the pristine one but is clearly dominant on black diamond because of the increased density of these states. These transitions are similar to those observed in Reference 8 by SPV on oxidized single-crystal diamond, but that were not detected on nanostructured boron-doped diamond (BDD) electrodes probably due to excessive charge recombination, which prevented the formation of SPV signal. In contrast, the absorption measured for BD sample under study is not affected by charge recombination. Moreover, it is also interesting to note that transitions from the C–OH surface states were determined by SPV at approximately 0.85–1.35 eV to the conduction band. These transitions can also increase absorption in this region, despite not being correlated with the unoccupied surface states measured by XAS. Such transitions can be particularly interesting for energy conversion, as the electrons in the conduction band are mobile and can be collected. The transition C at ~2.5–2.7 eV for the BD sample corresponds to the $\pi^*_{C=O}$ related surface states, also reported in Reference 8 at ~2.25–3 eV on the single crystal and 3.3 eV on the nanostructured BDD. The transition D (~2 eV) for the pristine sample can be associated with the presence of the same type of unoccupied states. Considering the contribution of the band-to-band excitation (named E), it is possible to state that this transition clearly dominates the absorption mechanism in the pristine sample, whereas the BD absorption is mostly influenced by the transitions involving different sp^2-like surface defects as depicted in Figure 3c.

It is important to note that this analysis has been performed assuming a homogeneous material with an effective absorption coefficient. Indeed, the BD sample consists of a complex structure made of a highly absorbing layer and a semi-transparent substrate. As a first approximation, this structure can be modeled as a thin-film layer on a thick substrate. This allows to estimate the absorption coefficient $\alpha_{BD}(h\nu)$ of the BD layer alone. Under this assumption,[44] the absorption coefficient of the BD is given by: $\alpha_{BD}(h\nu) = (d_{sub}/d_{BD}) \times (\alpha_{tot}(h\nu) - \alpha_{sub}(h\nu))$, where d_{sub} and d_{BD} are the thickness of the substrate below the BD layer and of the BD layer, respectively, whereas α_{tot} and α_{sub} are the measured absorption coefficients of the treated and pristine samples, respectively, as shown in Figure 3b. SI Figure S3 presented α_{BD} as calculated using the formula reported above, following the basic method described in Reference 42. On one hand, this confirms the optical transitions identified through correlation with XAS measurements; on the other hand, it reveals an extremely high absorption coefficient, ranging from 5×10^5 to 1×10^6 cm^{-1} in the visible spectrum. The values of thicknesses have been determined to be 475 and 0.25 μm for d_{sub} and d_{BD}, respectively, as measured by cross-sectional images on similar samples.[45] Although this model simplifies the optical behavior of the structure under study, it highlights a remarkable ~10^4-fold increase of the absorption coefficient along the investigated range. This finding underscores the potential of black diamond as a viable alternative to conventional semiconductors in photonic applications. More advanced models will be applied to further validate this important observation.

Although this study does not provide direct measurements of photogenerated carrier or recombination lifetimes, previous works (References 6 and 16) have correlated the effects of laser-induced nanostructuring on photocarrier generation through photoconductivity measurements. By comparing the results of the present study with those reported in the aforementioned works, in which the photoelectronic enhancement was drastically improved in the range 2.5–3.5 eV, the found surface states produced by nanostructuring do not have a large contribution in the photocarrier generation, which is probably limited by charge trapping. Instead, their role appears to be

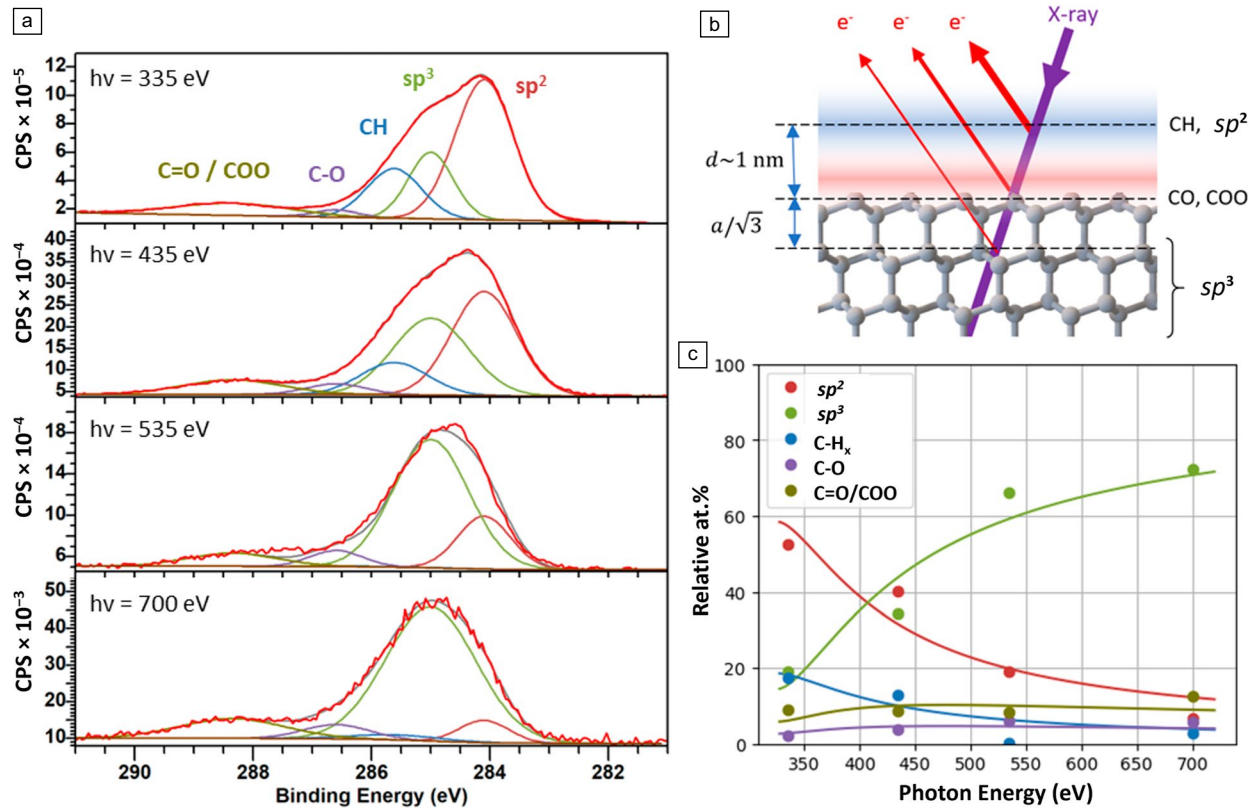

Figure 4. (a) *C 1s* x-ray photoemission line shapes measured at an incident photon energy of 335, 435, 535, and 700 eV on the black diamond (BD), resulting in *C 1s* photoelectron kinetic energies of 50, 150, 250, and 415 eV, respectively. (b) Cross section of the BD system considered by the model shown in Reference 44. (c) Evolution of the relative atomic percentage of each fitted component. CPS, counts per second.

limited to enhancing optical absorption. This suggests that the observed increase in photoconductivity is primarily due to the presence of vacancies[46] or defect states within the subsurface region which are additionally formed during laser processing. Obviously, this is a very important aspect to consider, understand, and optimize in the future for the design and engineering of the final device for PETE applications. Supporting this conclusion, previous studies have shown that a high density of surface defects, despite dominating light absorption, does not lead to a proportional increase in photocarrier generation due to charge trapping and/or scattering effects at the surface. Consequently, electronic conduction is primarily attributed to dopants and bulk defect states, such as those introduced by boron[42] or nitrogen[43] doping.

Finally, depth-resolved XPS measurements[47] were carried out on the BD to detect the different carbon species, using varying photon energies to tune the probing depth. The corresponding spectra are presented in **Figure** 4a. The increases in the photoelectron inelastic mean free path (IMFP) with increasing kinetic energy results in a decreased contribution of photoelectrons originating from the surface states compared to the bulk states. The evolution in the shape of *C 1s* peak line provides information on the depth of the carbon associated with each component. Global shift in the binding energy (BE), likely associated with small homogeneous charging and band bending, were corrected for the main peak to be positioned at 285.0 eV for all energies.

Spectral deconvolution of the *C 1s* peak line is composed of five peaks at 284.0, 285.0, 285.6, 286.5, and 288.5 eV associated, respectively, with C=C (sp^2 bonded carbon), C–C bonds in the diamond matrix (sp^3 bonded carbon), CH_x on the diamond surface, C–O bonds and C=O or COO bonds. The intensity of the different components is strongly dependent on the excitation energy.

Figure 4c shows the evolution of the calculated relative atomic percentage of each component as a function of the depth from the surface to the bulk. The strong increase of the sp^3 component correlates well with a bulk consisting of highly crystalline diamond while the dramatic decrease of the sp^2 component (C=C signal) clearly shows that these defects are only present at the very first atomic layers. Moreover, the CH signal also seems to decrease with the photon energy, which suggests it is located at the surface of the diamond. Conversely, the CO and COO signals appear to slightly increase, indicating that they are surface states under some adsorbed molecules.

The evolution of the signals can be fitted through the use of a model developed previously for different systems,[47] aiming to reconstruct the ultimate terminal surface layers.

Surface roughness induced by the nanoscale corrugation of the 1D-LIPSS could influence the effective escape depth of photoelectrons and affect the quantitative interpretation of the depth profiles. Therefore, the assumption of a flat and homogeneous surface in the depth-resolved XPS analysis represents a simplification may slightly overestimate the density of surface states and defects. However, based on the homogeneity of the surface states determined by TERS and the large scale of the LIPSS with respect to the XPS probing depth (i.e., a few nanometers), we consider that it is reasonable to consider a bare diamond surface in the molecular model, not taking account the nanostructuring. In fact, depth-resolved XPS, performed at the kinetic energies used in this work, probes only the first few nanometers of the surface, a scale much smaller than the few hundred nanometers of surface structuration.[48] The only impact on the modeling would be a statistical variation of the exit angle, which influences the calculated depth of each bonding configuration in the model fit. In practice, the dominant exposed surface behaves similarly to a flat one, meaning the estimation of surface state depths remains relevant. The evaluation of the model is shown in Figure 4b, for which only two categories of populations have been considered based on the XPS results: CH/C and CO–C. The model suggests that the diamond surface is oxidized with approximately 70% COO/C=O and 30% CO and overlaid by a hydrocarbon layer (~1 nm) composed of ~25% C-H and ~75% sp^2 carbon. The analysis agrees with the results of the previous investigations, thus indicating that the sp^2 contribution, always present in oxidized diamond surfaces, is enhanced for BD (recalling that the surface is chemically oxidized after the laser treatment to etch the graphitic debris formed during the texturing process) and directly involved in the subbandgap optical absorption.

Finally, considering that this study has been carried out to understand the feasibility of such material for PETE applications, it is possible to conclude that the observed enhancement in visible light absorption and surface defect states formation suggest the potential application as PETE cathodes, even if the long-term thermal and structural stability of such engineered states remains to be demonstrated. Future studies will involve device-level fabrication and testing, including evaluations under high-temperature and high-flux conditions relevant to PETE systems.

Conclusion

This study highlighted that the significant enhancement of the optical subbandgap absorption for 1D-LIPSS BD plates derives from the formation of an enhanced density of states in the bandgap of nanostructured diamond surfaces, thus indicating that the diffraction trapping is not the only contribution for this enhancement. The nature of these defects is ascribable to sp^2-like defects on the diamond surface after the fs-laser treatment, by finding a strong correlation between these XAS and TERS measurements and PDS analysis. A basic method indicates that the BD layer alone could reach extremely high values of absorption coefficient, thus indicating the thinner samples can be used for optical devices. Finally, resolved XPS showed that sp^2-related defects are confined in the upmost layers of the BD surface. Although the long-term stability of the structure still needs to be demonstrated, this work has provided insights into the role of surface defects, also in relation to the mechanism of photo-carrier generation. In the future, fabrication strategies for controlling the presence and the effects of this kind of defects should be implemented to optimize the 1D-LIPSS BD material for opto-electronic and solar-energy-conversion applications, and the extension of the fs-laser technique to other wide bandgap semiconductors would represent a valuable direction for future works.

Acknowledgments

A.B. acknowledges the funding by the CNR Short Term Mobility (STM) 2019 grant, allowing to perform part of the work at Stanford University. A.B. and A.S. thank the Italian Scientists and Scholars in North America Foundation (ISSNAF) for giving them the opportunity to share knowledge and ideas at the basis of this work. T.P. and A.C. acknowledge the funding from a Freigeist Fellowship from the Volkswagen Foundation (n° 89592).

Author contributions

A.B. and D.M.T. conceived the work; A.B, M.G., S.O., and D.M.T. fabricated the samples under investigation; A.C. and T.P. performed XAS and XPS measurements and developed the model; E.B. and V.V. performed the TERS measurements; B.L.C. and A.S. performed the PDS measurements. A.B., A.C., and T.P. contributed to the writing of the original draft. All the authors contributed to the review and editing of the draft.

Funding

Open access funding provided by Consiglio Nazionale Delle Ricerche (CNR) within the CRUI-CARE Agreement. Funded by the European Union-Next Generation EU, Mission 4 Component 1, CUP B53D23015370006, MUR project SPEEDHY (2022J9CEFM).

Data availability

Data will be made available on request.

Conflict of interest

The authors declare that they have no known competing financial interests or personal relationships that could have appeared to influence the work reported in this article.

Supplementary information

The online version contains supplementary material available at https://doi.org/10.1557/s43577-025-00971-2.

References

1. J.W. Schwede, I. Bargatin, D.C. Riley, B.E. Hardin, S.J. Rosenthal, Y. Sun, F. Schmitt, P. Pianetta, R.T. Howe, Z.X. Shen, N.A. Melosh, *Nat. Mater.* **9**, 762 (2010). https://doi.org/10.1038/nmat2814
2. G. Segev, Y. Rosenwaks, A. Kribus, *Sol. Energy Mater. Sol. Cells* **140**, 464 (2015). https://doi.org/10.1016/j.solmat.2015.05.001
3. M.F. Campbell, T.J. Celenza, F. Schmitt, J.W. Schwede, I. Bargatin, *Adv. Sci.* **8**(9), 2003812 (2021). https://doi.org/10.1002/advs.202003812
4. A. Bellucci, M. Girolami, M. Mastellone, S. Orlando, R. Polini, A. Santagata, V. Serpente, V. Valentini, D.M. Trucchi, *Nanotechnology* **32**, 024002 (2021). https://doi.org/10.1088/1361-6528/abba57
5. P. Calvani, A. Bellucci, M. Girolami, S. Orlando, V. Valentini, A. Lettino, D.M. Trucchi, *Appl. Phys. A* **117**, 25 (2014). https://doi.org/10.1007/s00339-014-8311-9
6. A. Bellucci, P. Calvani, M. Girolami, S. Orlando, R. Polini, D.M. Trucchi, *Appl. Surf. Sci.* **380**, 8 (2016). https://doi.org/10.1016/j.apsusc.2016.02.107
7. M. Mastellone, A. Bellucci, M. Girolami, V. Serpente, R. Polini, S. Orlando, A. Santagata, E. Sani, F. Hitzel, D.M. Trucchi, *Nano Lett.* **21**, 4477 (2021). https://doi.org/10.1021/acs.nanolett.1c01310
8. A. Chemin, I. Levine, M. Rusu, R. Vaujour, P. Knittel, P. Reinke, K. Hinrichs, T. Unold, T. Dittrich, T. Petit, *Small Methods* **7**, e2300423 (2023). https://doi.org/10.1002/smtd.202300423
9. D.M. Trucchi, A. Bellucci, M. Girolami, M. Mastellone, S. Orlando, *Coatings* (Basel) **7**, 185 (2017). https://doi.org/10.3390/coatings7110185
10. A. Bellucci, M. Girolami, P. Calvani, S. Michaelson, A. Hofmann, V. Carcelen, D.M. Trucchi, *IEEE Trans. Nanotechnol.* **15**, 862 (2016). https://doi.org/10.1109/TNANO.2016.2566674
11. M. Girolami, L. Criante, F. Di Fonzo, S.L. Turco, A. Mezzetti, A. Notargiacomo, M. Pea, A. Bellucci, P. Calvani, V. Valentini, D.M. Trucchi, *Carbon* **111**, 48 (2017). https://doi.org/10.1016/j.carbon.2016.09.061
12. X. Shi, N. Coca-López, J. Janik, A. Hartschuh, *Chem. Rev.* **117**, 4945 (2017). https://doi.org/10.1021/acs.chemrev.6b00640
13. Z.D. Schultz, S.J. Stranick, I.W. Levin, *Appl. Spectrosc.* **62**, 1173 (2008). https://doi.org/10.1366/000370208786401635
14. N. Kumar, S. Mignuzzi, W. Su, D. Roy, *EPJ Tech. Instrum.* **2**, 9 (2015). https://doi.org/10.1140/epjti/s40485-015-0019-5
15. K. Vandewal, S. Albrecht, E.T. Hoke, K.R. Graham, J. Widmer, J.D. Douglas, M. Schubert, W.R. Mateker, J.T. Bloking, G.F. Burkhard, A. Sellinger, *Nat. Mater.* **13**, 63 (2014). https://doi.org/10.1038/nmat3807
16. P. Calvani, A. Bellucci, M. Girolami, S. Orlando, V. Valentini, R. Polini, D.M. Trucchi, *Carbon* **105**, 401 (2016). https://doi.org/10.1016/j.carbon.2016.04.017
17. A. Rosenkranz, L. Freeman, S. Fleischmann, F. Lasserre, Y. Fainman, F.E. Talke, *Carbon* **132**, 495 (2018). https://doi.org/10.1016/j.carbon.2018.02.088
18. L. Hu, Y. Guo, S. Du, S. Tian, J. Li, C. Gu, *Diam. Relat. Mater.* **116**, 108415 (2021). https://doi.org/10.1016/j.diamond.2021.108415
19. A.C. Ferrari, J. Robertson, A.C. Ferrari, J. Robertson, *Philos. Trans. R. Soc. Lond. A Math. Phys. Eng. Sci.* **362**, 2477 (2004). https://doi.org/10.1098/rsta.2004.1452
20. A.C. Ferrari, J. Robertson, *Phys. Rev. B* **63**, 121405 (2001). https://doi.org/10.1103/PhysRevB.63.121405
21. I. Harada, Y. Furukawa, M. Tasumi, H. Shirakawa, S. Ikeda, *J. Chem. Phys.* **73**, 4746 (1980). https://doi.org/10.1063/1.440007
22. A.C. Ferrari, *Diam. Relat. Mater.* **11**, 1053 (2002). https://doi.org/10.1016/S0925-9635(01)00730-0
23. M. Mermoux, A. Crisci, T. Petit, H.A. Girard, J.-C. Arnault, *J. Phys. Chem. C* **118**, 23415 (2014). https://doi.org/10.1021/jp507377z
24. S. Prawer, R.J. Nemanich, *Philos. Trans. A. Math. Phys. Eng. Sci.* **362**, 2537 (2004)
25. J.S. Tu, E. Perevedentseva, P.H. Chung, C.L. Cheng, *J. Chem. Phys.* **125**, 174713 (2006). https://doi.org/10.1063/1.2370880
26. J.F. Morar, F.J. Himpsel, G. Hollinger, G. Hughes, J.L. Jordan, *Phys. Rev. Lett.* **54**, 1960 (1985). https://doi.org/10.1103/PhysRevLett.54.1960
27. Z. Shpilman, I. Gouzman, T.K. Minton, L. Shen, A. Stacey, J. Orwa, S. Prawer, B.C.C. Cowie, A. Hoffman, *Diam. Relat. Mater.* **45**, 20 (2014). https://doi.org/10.1016/j.diamond.2014.03.004
28. A. Laikhtman, I. Gouzman, A. Hoffman, G. Comtet, L. Hellner, G. Dujardin, *J. Appl. Phys.* **86**, 4192 (1999). https://doi.org/10.1063/1.371346
29. A. Stacey, N. Dontschuk, J.P. Chou, D.A. Broadway, A.K. Schenk, M.J. Sear, J.P. Tetienne, A. Hoffman, S. Prawer, C.I. Pakes, A. Tadich, *Adv. Mater. Interfaces* **6**, 1801449 (2019). https://doi.org/10.1002/admi.201801449
30. A. Laikhtman, A. Hoffman, *Surf. Sci.* **522**, L1 (2003). https://doi.org/10.1016/S0039-6028(02)02409-3
31. A. Hoffman, G. Comtet, L. Hellner, G. Dujardin, M. Petravic, *Appl. Phys. Lett.* **73**, 1152 (1998). https://doi.org/10.1063/1.122113
32. K.C. Prince, R. Richter, M. de Simone, M. Alagia, M. Coreno, *J. Phys. Chem. A* **107**, 1955 (2003). https://doi.org/10.1021/jp0219045
33. C.D. Clark, P.J. Dean, P.V. Harris, *Proc. R. Soc. A Math. Phys. Eng. Sci.* **277**, 312 (1964). https://doi.org/10.1098/rspa.1964.0025
34. T. Dittrich, *AIP Adv.* **12**(6), 065206 (2022). https://doi.org/10.1063/5.0089398
35. T. Dittrich, S. Fengler, *Semicond. Sci. Technol.* **38**(1), 015015 (2022). https://doi.org/10.1088/1361-6641/aca788
36. A.C. Boccara, D. Fournier, J. Badoz, *Appl. Phys. Lett.* **36**, 130 (1980). https://doi.org/10.1063/1.91395
37. A. Mandelis, *J. Appl. Phys.* **54**, 3404 (1983). https://doi.org/10.1063/1.332454
38. S. Dou, H. Xu, J. Zhao, K. Zhang, N. Li, Y. Lin, L. Pan, Y. Li, *Adv. Mater.* **33**, 2000697 (2021). https://doi.org/10.1002/adma.202000697
39. H.K. Raut, V.A. Ganesh, A.S. Nair, S. Ramakrishna, *Energy Environ. Sci.* **4**, 3779 (2011). https://doi.org/10.1039/C1EE01297E
40. K. Tanaka, T. Gotoh, N. Yoshida, S. Nonomura, *J. Appl. Phys.* **91**(1), 125 (2002). https://doi.org/10.1063/1.1426252
41. M. Nesládek, M. Vaněček, J. Rosa, C. Quaeyhaegens, L.M. Stals, *Diam. Relat. Mater.* **4**, 697 (1995). https://doi.org/10.1016/0925-9635(94)05248-4
42. W. Gajewski, P. Achatz, O.A. Williams, K. Haenen, E. Bustarret, M. Stutzmann, J.A. Garrido, *Phys. Rev. B* **79**, 045206 (2009). https://doi.org/10.1103/PhysRevB.79.045206
43. E. Rohrer, O.C.F. Graeff, R. Janssen, C.E. Nebel, M. Stutzmann, H. Güttler, R. Zachai, *Phys. Rev. B* **54**, 7874 (1996). https://doi.org/10.1103/PhysRevB.54.7874
44. M. Cesaria, A.P. Caricato, M. Martino, *J. Opt.* **17**, 025610 (2015). https://doi.org/10.1088/2040-8978/17/2/025610
45. S. Amoruso, A. Andreone, A. Bellucci, C. Koral, M. Girolami, M. Mastellone, S. Mou, S. Orlando, G.P. Papari, D. Paparo, R. Polini, *Carbon* **163**, 197 (2020). https://doi.org/10.1016/j.carbon.2020.03.023
46. X. Dong, Y. Wang, X. Song, *J. Phys. Condens. Matter* **32**, 165502 (2020). https://doi.org/10.1088/1361-648X/ab6740
47. A. Chemin, M.K. Kuntumalla, M. Brzhezinskaya, T. Petit, A. Hoffman, *Appl. Surf. Sci.* **661**, 160082 (2024). https://doi.org/10.1016/j.apsusc.2024.160082
48. Z. Dessoliers, A. Chemin, G. Valurouthu, R. Lord, T. Bilyk, Y. Gogotsi, V. Mauchamp, T. Petit, *Adv. Mater. Interfaces* **12**(13), 2500391 (2025). https://doi.org/10.1002/admi.202500391

Publisher's Note